ADVANCED MATERIALS
www.advmat.de



# Knotted Artificial Muscles for Bio-Mimetic Actuation under Deepwater

*Wenhui Chen, Dezhong Tong, Linghan Meng, Bowen Tan, Ruochen Lan, Qifeng Zhang, Huai Yang,* Cong Wang,* and Ke Liu**

**Muscles featuring high frequency and high stroke linear actuation are essential for animals to achieve superior maneuverability, agility, and environmental adaptability. Artificial muscles are yet to match their biological counterparts, due to inferior actuation speed, magnitude, mode, or adaptability. Inspired by the hierarchical structure of natural muscles, artificial muscles are created that are powerful, responsive, robust, and adaptable. The artificial muscles consist of knots braided from 3D printed liquid crystal elastomer fibers and thin heating threads. The unique hierarchical, braided knot structure offers amplified linear stroke, force rate, and damage-tolerance, as verified by both numerical simulations and experiments. In particular, the square knotted artificial muscle shows reliable cycles of actuation at 1 Hz in 3000m depth underwater. Potential application is demonstrated by propelling a model boat. Looking ahead, the knotted artificial muscles can empower novel biomedical devices and soft robots to explore various environments, from inside human body to the mysterious deep sea.**

## 1. Introduction

Animal muscles have been the most efficient soft actuators in nature with outstanding actuation properties,[1–5] which excite the development of artificial muscles in man-made systems, such as soft robots[6–8] and biomedical devices.[9,10]

W. Chen, B. Tan, K. Liu
Department of Advanced Manufacturing and Robotics
Peking University
No. 5 Yiheyuan Rd., Beijing 100871, China
E-mail: liuke@pku.edu.cn

D. Tong
Department of Mechanical and Aerospace Engineering
University of California, Los Angeles
405 Hilgard Ave., Los Angeles, California 90095, USA

L. Meng, Q. Zhang, C. Wang
Shenyang Institute of Automation
Chinese Academy of Sciences
No. 135 Chuangxin Rd., Shenyang 110169, China
E-mail: wangcong2@sia.cn

R. Lan, H. Yang
School of Materials Science and Engineering
Peking University
No. 5 Yiheyuan Rd., Beijing 100871, China
E-mail: yanghuai@pku.edu.cn

The ORCID identification number(s) for the author(s) of this article can be found under https://doi.org/10.1002/adma.202400763

**DOI: 10.1002/adma.202400763**

The performance of artificial muscles is highly dependent on their material selections.[11–14] Shape memory polymers (SMPs),[15,16] hydrogels,[17,18] dielectric elastomers (DEs),[19,20] and liquid crystal elastomers (LCEs)[21–23] have been the most explored active materials for preparing artificial muscles. Among these materials, LCEs stand out to be the most similar to natural muscles, owing to their large reversible strain,[24,25] mechanical robustness,[26,27] flexible actuation modes,[28–31] and scalable force output.[32,33]

The large deformation of most LCEs results from the nematic-isotropic phase transition driven by the changing orientation of liquid crystal mesogens.[28,34–36] However, this thermal-induced phase transition depends on the efficiency of heat transfer within the material, which is the main reason for the slow actuation strain rate of most LCE artificial muscles. To achieve faster strain rate, innovations to improve heating and cooling efficiency of the artificial muscle is necessary. Besides exhaustively enumerating different chemical compositions, there are still much to be explored on the structural design of the LCE artificial muscles. As we examine the details of natural muscles, except for the highly efficient actin and myosin proteins, their hierarchical structures, ranging from myofabrils to muscle fibers and to fasciculi, are also critical to their overall performance.[2,37] In contrast, little attention has been paid to how the structures of LCE artificial muscles may influence their actuation strain and strain rate.

Inspired by the structure of natural muscles, we invent an effective method for creating adaptable and reliable artificial muscles by braiding 3D printed LCE fibers and commercial heating threads into architected bundles (**Figure 1**a). In particular, it has been noticed that if the LCEs are made to very thin fibers,[24,29] they are capable of super fast actuation comparable to that of natural muscle fibers. This is because the large specific surface area of fibers significantly improves the heat absorption and dissipation of the LCE material with external heat sources and sinks. However, a single fiber cannot generate enough force for practical applications, and it is not clear how to maintain the superior performance of individual LCE fibers when they are grouped, as well as how to integrate proper heating method.[12] In this work, we braid these thin fibers together with thin heating threads to achieve an integral artificial muscle bundle to produce scalable actuation forces. Unlike the woven LCE fabrics for bi-axial

 

ADVANCED MATERIALS
www.advmat.de

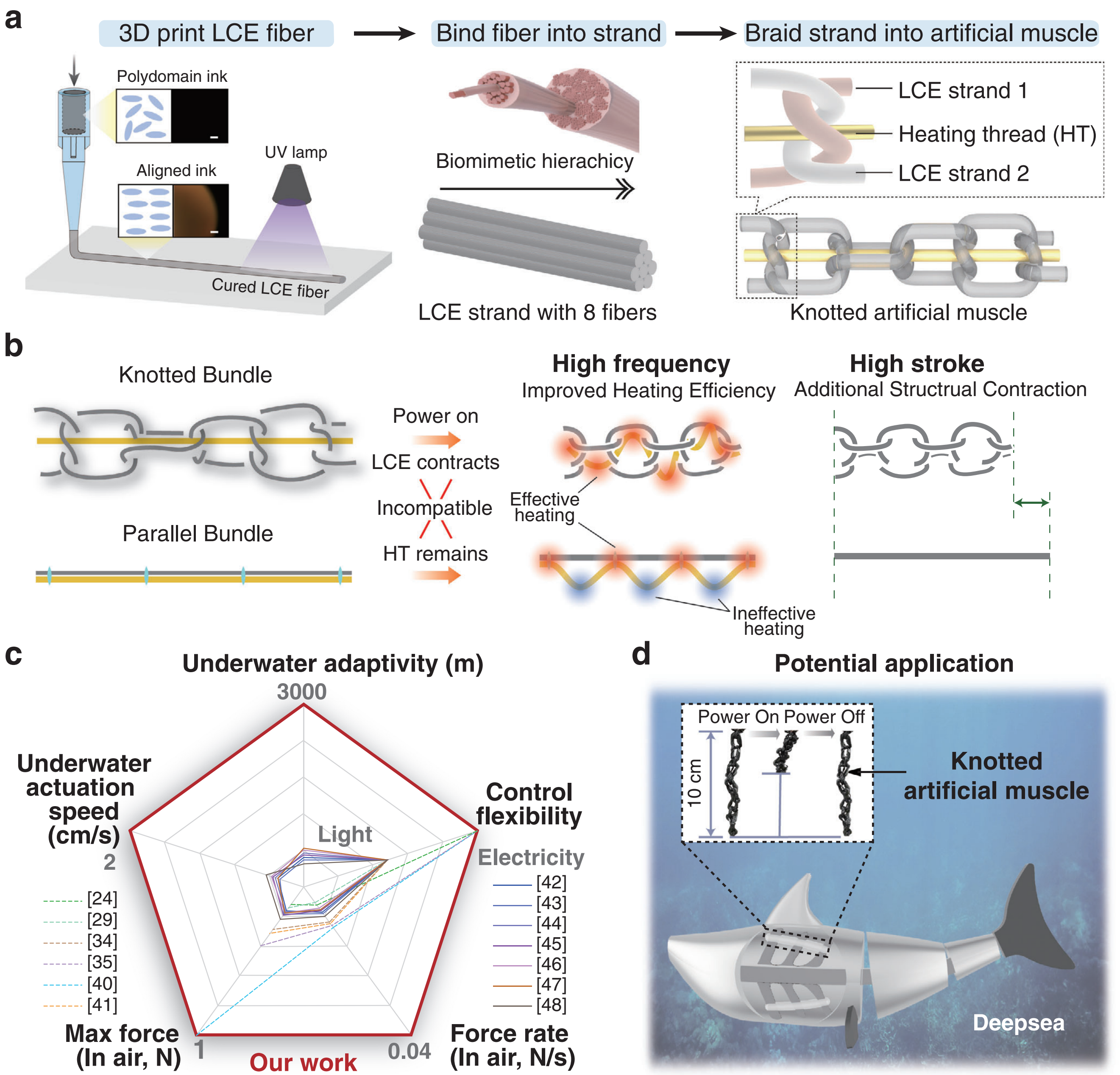


**Figure 1.** Design and fabrication of the knotted artificial muscles. a) Fabrication process of knotted artificial muscles. LCE fibers are manufactured by 3D printing, and then grouped into strands. The strands are braided with heating threads into bundles of artificial muscles. The two insets are the POM images (scale bar, 200µm) before and after the LCE is printed, showing the alignment of the liquid crystals. b) The knotted structure greatly amplifies the actuation performance of the LCE material, leading to high stroke and high frequency actuation. c) Comparison of the actuation performance of this work and other existing LCE based actuators.[24,29,34,35,40–48] The dashed lines refer to literatures that do not present underwater measurements, while the solid lines refer to literatures that include underwater measurements. The scales of the axes are not linear near the origin. Small values are exaggerated for better visualization. Some actuation properties are not directly presented in the original papers, and thus they are inferred from known information. d) Potential application of knotted artificial muscles on soft robot working in deepsea.

actuation,[26,38,39] our knotted bundles are for improving the actuation performance of uni-axial artificial muscles (Figure 1b), aiming at high stroke, high frequency, linear actuation for underwater applications.

Most artificial muscles made of smart materials, including LCEs, have not been experimented in underwater environment, especially for deepwater (>100m).[34,35,40,49,50] Nevertheless, as implied by the many soft-bodied animals living in deep seas,[51,52] smart material based soft actuators seem to be intrinsically suitable for deepwater applications. That is because the material actuates the body by deforming itself, and thus there is no need to leave empty space inside for moving components like in

ADVANCED MATERIALS
www.advmat.de

mechanical or pneumatic actuators, which can be fragile under high pressure. While it has been demonstrated that DE-based artificial muscles successfully achieved bending actuation in the Mariana Trench,[53] there has been no such breakthrough for LCEs that are capable of generating large linear actuation.

We evaluate three kinds of braiding styles, namely, the Lark's head knot, the square knot and the three-strand knot, and compare them with the parallel bundle, where LCE fibers and heating thread are simply grouped together in parallel with each other. All three knotted ones outperform the parallel bundle in air due to the additional structural contraction, among which the square knotted artificial muscles display the fastest and largest actuation. We then test the performance of the square knotted artificial muscles in water, against both shallow and deepwater environment. The deepwater experiment is conducted in a pressure vessel with a pressure of 30MPa (equivalent to a depth of 3000m), which is the first time that an LCE-based soft actuator is tested in such extreme environment. The square knotted artificial muscles present better deepwater actuation performance in terms of linear actuation strain and damage-tolerance than DE-based artificial muscle[53] (Table S1, Supporting Information). Compared to other existing LCE-based actuators, the square knotted artificial muscles also excel at underwater adaptivity, maximum achieved force, and force rate (Figure 1c; Table S2, Supporting Information). Equipped with such knotted artificial muscles, a small boat is successfully propelled, shedding light on potential underwater applications of the knotted artificial muscles (Figure 1d).

## 2. Results and Discussion

### 2.1. Manufacturing, Mechanics, and and Mechanism of Knotted Artificial Muscles

The LCE fibers are 3D printed using a customized setup. The LCE ink is synthesized by a straightforward, one-pot methodology using commercially available precursors (Figure S1a, Supporting Information). To reduce the input power for actuation, we first regulate the amount of thermal polymerization agent, catalyst dipropylamine (DPA), in the LCE ink. Larger amount of DPA results in larger actuation strain at lower actuation temperature of the LCE materials (Figure S1b– d, Supporting Information). As the amount of DPA increases from 0.01 to 0.05g in 1g of the LCE ink, the nematic-to-isotropic transition temperature ($T_{NI}$) decreases from 78 to 66°C (Figure S1b,c, Supporting Information), while the actuation strain keeps increasing (Figure S1d, Supporting Information). On the other hand, the tensile strength of the LCE fibers decreases as the amount of DPA increases (Figure S1e, Supporting Information). Considering the overall performance that includes actuation temperature, actuation strain, and tensile strength, we choose a concentration of 0.02wt.% DPA for the preparation of the printable LCE ink.

The viscosity of the LCE ink decreases with the increase of the shear rate during extrusion (Figure S1f, Supporting Information). The lower the viscosity, the larger the diameter of the extruded LCE fibers. Hence, by adjusting the feeding pressure of the ink, we can control the diameter of the printed LCE fibers, within a range of 160 to 400µm (**Figure** 2a). In general, thinner LCE fibers display faster heating and cooling efficiency, resulting in larger actuation strain and faster strain rate (Figure 2b; Figure S2, Supporting Information). However, thinner LCE fibers are printed in worse shape uniformity (Figure 2a, inner) and may rapture due to local stress concentration in practice. Thus, for the artificial muscles, we select LCE fibers with a diameter of 300µm, which can be printed in a uniform thickness, and display relatively optimal actuation properties (actuation strain: 42%, actuation strain rate: 16%/s at 120°C).

Except for the LCE fibers, we also need to choose suitable heating threads for the knotted artificial muscles. Convenient candidates for heating threads include pure metal threads, threads mixed with metal and other materials, and pure carbon fibers.[54–56] We compare nickel-chromium (NiCr) wires, carbon fibers (CF), and stainless steel fiber yarn (SSFY) as the heating threads. The NiCr wires is representative among commonly used pure metal heating threads, including copper threads, silver threads, and tungsten threads (Figure S3a–c, Supporting Information). The CF is the representative of commonly used non-metallic heating element. The SSFY is a commercially available heating thread that is durable with a negligible bending stiffness. Among these three types of heating threads, the SSFY threads have the smallest resistance at 0.4Ωcm$^{-1}$ (Figure S3d, Supporting Information), and they can endure the highest temperature with the fastest heating and cooling rate, given the same voltage input (**Figure** 3e,f). At a voltage of 4V, the 10-cm SSFY thread heats up to about 100°C with a heating rate of 15°Cs$^{-1}$, and it cools down at a speed of 10°Cs$^{-1}$ in air when the voltage is turned off. The SSFY threads are also more flexible compared to the other candidates, leading to less constraint on the shrinkage of the LCE fibers in the knotted bundles. Therefore, the SSFY is chosen as the heating thread in this work. Once the LCE fibers and the heating threads are determined, we braid them together in bundles to create artificial muscles. Three different braiding styles are tested (namely the Lark's head knot, square knot, and three strand braid knot), as well as the parallel bundle, each results in distinct topology, with the same distance between knots of 4mm (Figure 2c; Movie S1, Supporting Information).

The four different designs of artificial muscles are tested to lift a weight of 1g, given a continuous current of 0.8A (Figure 2d,e; Movie S2, Supporting Information). During one heating and cooling cycle, the knotted bundles, particularly those braided with square knots, exhibit significant improvements in actuation strain and actuation strain rate, compared to the parallel bundle (Figure 2d,e; Movies S2 and S3, Supporting Information). The actuation strain is defined as the the contracted length over the original length of the actuator. The improved actuation performance of the knotted bundles is attributed to their responsive temperature changes during the power-on and power-off phases, detected using an infrared thermal camera (Figure S4a, Supporting Information). Among the four designs, the square knotted bundle exhibits the highest heating rate and peak temperature, and the parallel bundle shows the lowest heating rate and peak temperature (Figure 2f; Figure S4b, Supporting Information). Additionally, the square knotted artificial muscle demonstrates superior actuation strain, strain rate and actuation stress given the same input power and the number of LCE fibers (Figure 2f; Figure S5, Supporting Information).

Under a uniform shrinkage of the LCE fibers, the overall length of the artificial muscle bundle decreases. Because the heating threads cannot contract, they buckle out of the bundle,

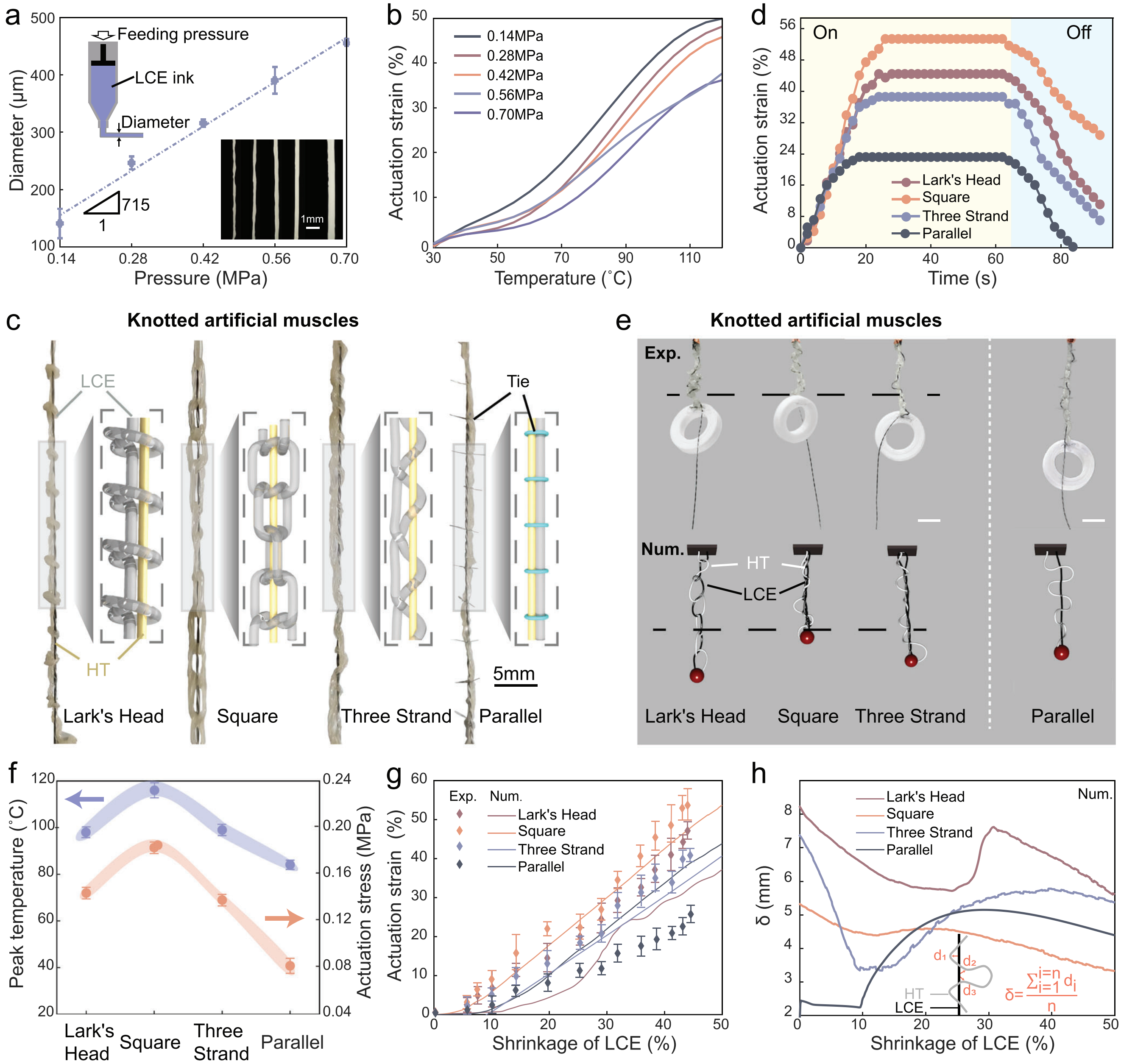


**Figure 2.** Construction, actuation performance, and thermal properties of the knotted artificial muscles. a) Diameter of the LCE fibers versus feeding pressure. The inset in the upper left corner is the process of regulating the diameter of LCE fibers. The inset in the lower right corner shows the photographs of LCE fibers printed under the feeding pressures of 0.14, 0.28, 0.42, 0.56, and 0.70MPa, respectively, from left to right. The dotdashed line refers to the linearly fitted relationship. The error bars extend to one standard deviation. b) Actuation strain of LCE fibers printed at different feeding pressures versus temperature. The lines show the average values of three samples. c) Photographs and structural designs of the three kinds of knotted bundles and a parallel bundle. d) The actuation strain of different styles of knotted bundles during the process of turning on and off the power supply. The lines show the average values of three samples. e) Final states of the knotted bundles during actuation in experiments and numerical simulations. f) Peak temperatures and actuation stresses of the knotted bundles. The actuation stress is calculated as the actuation force divided by the net cross-sectional area of the LCE fibers. The shaded areas extend to one standard deviation. The temperature monitoring focuses on the overall actuator.g) Actuation strain of the knotted bundles versus shrinkage of the LCE fibers in experiments and numerical simulations. The error bars extend to one standard deviation. h) Numerical results of average effective distance between the LCE strands and the corresponding heating thread versus shrinkage of the LCE fibers. The effective distance is defined as the closest distance from a point on the LCE strand to the heating thread, as illustrated by the inset.

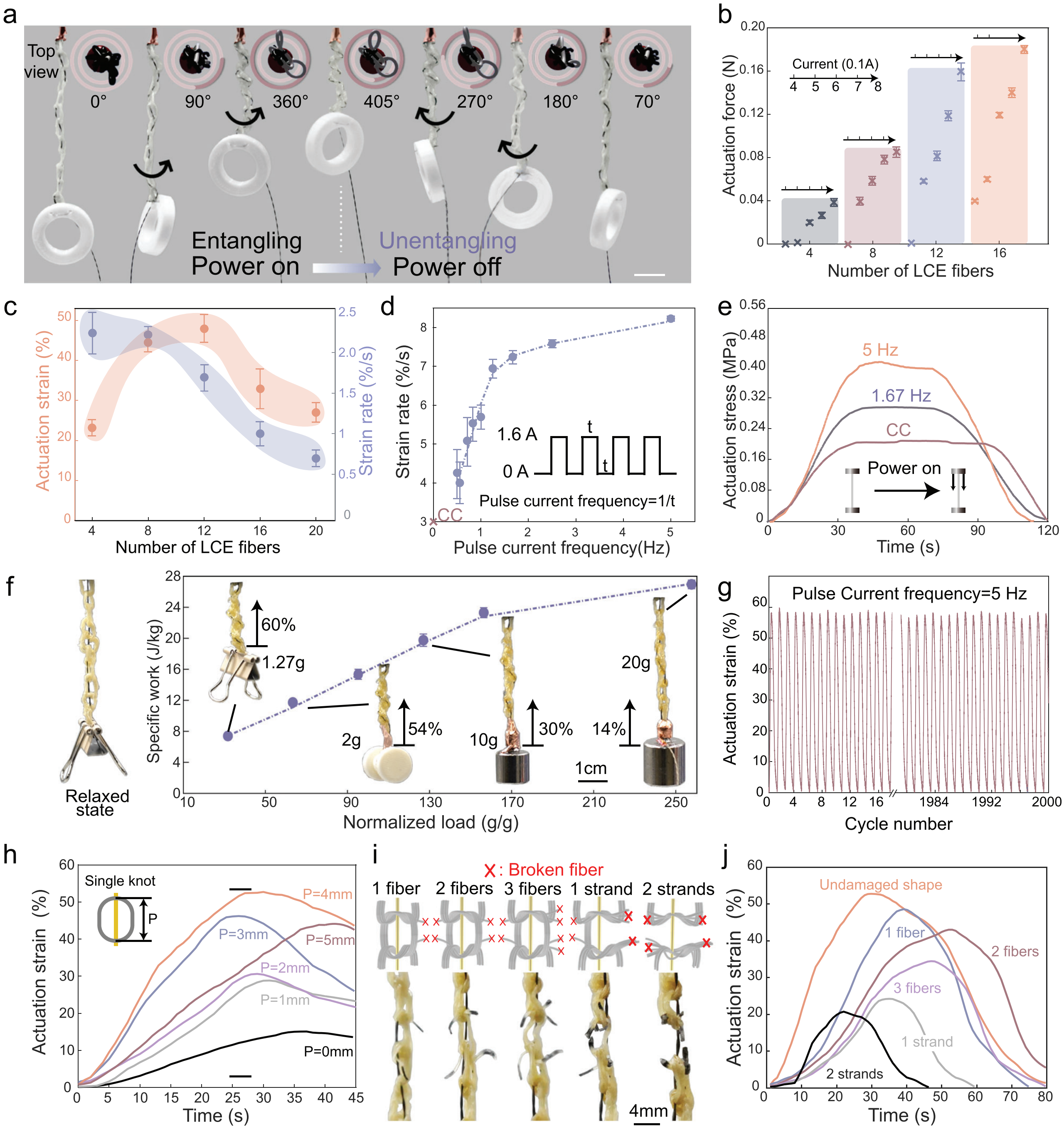


**Figure 3.** Extended analyses on the actuation performance of the square knotted artificial muscles. a) Deformation process of square knotted bundle with power turned on and off. The insets on the top are the top views of deformed knotted artificial muscle in numerical simulations with labeled twisting angles. b) Actuation force, c) actuation strain and strain rate of square knotted bundles with different strands of LCE fibers versus the number of LCE fibers under the stimulation of current of 0.8A. The error bars extend to one standard deviation. d) Actuation strain rate of square knotted bundles with 8-stranded fibers under pulse current stimulation. The application method of pulse current is illustrated in the inset. The error bars extend to one standard deviation. The dot-dashed line refers to the fitted quadratic relationship. e) Actuation stress of 8-stranded bundles under the stimulation of continuous current and pulse current of 1.67 and 5Hz. The testing process is as shown in the inset. The lines show the average values of three samples. f) Specific work as a function of normalized load for a square knotted bundle with 8-stranded bundles for three actuation cycles. The weight of LCE bundle in artificial muscle is 0.0769g. The insets are photographs of the square knotted bundle in different loaded states. The error bars extend to one standard deviation. The dot-dashed line refers to the fitted cubic relationship. g) Actuation strain of 2000 cycles for square knotted bundles with eight-stranded fibers actuating with a 1g hanging weight at a pulse current frequency of 5Hz. h) Comparison of actuation strain of the square knotted bundle with various pitch distance between knots. Each line shows the average value of three samples. i) A collection of typical damage scenario of the knotted artificial muscle with different number of broken fibers. j) Robust actuation performance of artificial muscles under different damaged scenario. Each line shows the average value of three samples.

 

forming a new structure with the shrank LCE fibers. It is observed that the topology of the braiding style has notable influence on the resultant new structure, and different structures possess different longitudinal lengths. In other words, different braiding styles lead to different amounts of structural contraction, under the same shrinkage of the LCE fibers. Numerical simulations verify that the square knotted bundle has the largest structural contraction compared to other braiding styles, even surpassing the actuation strain of the LCE fibers, which is consistent with the experimental results (Figure 2e,g; Movie S3, Supporting Information). In addition, the buckling of the heating threads compromises the heating efficiency due to the increased distance between the heating threads and the LCE fibers. The numerical simulations reveal that the square knotted bundle has the smallest average effective distance ($\delta$) between the LCE strands and the heating threads over most range of the actuation process, especially when the shrinkage of the LCE fibers is more than 20% (Figure 2h). Both experiments and simulations show that for the square knotted bundles, when power is turned on, the LCE fibers contract and entangle with heating thread into a spiral structure. This spiral entanglement results in enhanced heating efficiency and, consequently, an increase in both actuation strain and strain rate (Figure 3a). Therefore, we may conclude that the square knotted artificial muscle bundle shows the best actuation performance among all designs mainly due to the following two facts: 1) the largest structural contraction; 2) the least compromised heating efficiency. Details of the numerical simulations can be found in the Supporting Information.

### 2.2. Actuation Performance of Square Knotted Artificial Muscles

In the previous samples, 8 LCE fibers make up one LCE strand, and several strands are braided into one artificial muscle bundle. Now focusing on the best-performing square knotted bundles, we investigate how the number of LCE fibers in each LCE strand may affect the overall actuation performance. First, the total actuation force shows a monotonic increase with the number of fibers when heated with both ends fixed. We also fabricate a bundle of artificial muscle that generate a maximum force over 1N with a force rate of 0.04Ns$^{-1}$ (Figure S6, Supporting Information). Such excellent scalability is critical for practical applications (Figure 3b). Second, the relationship between actuation strain and the number of LCE fibers in each strand exhibits a nonlinear trend (Figure 3c), tightened by a small weight of 1.27g. Third, the relationship between the force rate and number of LCE fibers shows a similar trend as the actuation strain (Figure S7a, Supporting Information). Fourth, the actuation strain rate decreases with the number of LCE fibers in each strand (Figure 3c). The reason for this trend may be attributed to the decreased heating efficiency due to the increased number of LCE fibers, while keeping a single heating thread (Figure S8, Supporting Information). Therefore, taking into account all aspects of the actuation performance, we conclude that the square knotted bundle containing 8 fibers is the optimal design for in-air actuation.

In general, larger input current leads to higher heating speed, and thus faster actuation. However, we cannot keep a large magnitude of current for a long period because otherwise the LCE material would disintegrate due to overheating. Observing the fact that the cooling speed of the square knotted bundle is much slower than the strain rate (Figure S7b, Supporting Information), we propose a new heating method by pulse current to further accelerate the actuation strain rate. With the stimulation of pulse current at 1.6A with a duty cycle of 50%, the actuation strain rate increases with the increasing of pulse current frequency and reaches about 10%s$^{-1}$ at 5Hz (Figure 3d). Meanwhile, the actuation strain increases as well and reaches 60% at 5Hz (Figure S9a; Movie S4, Supporting Information). In other words, keeping the same output power with continuous current of 0.8A, the pulse current of 1.6A at 5Hz enables the artificial muscle to achieve an increase of nearly 15% in actuation strain and 300% in actuation strain rate. A possible reason for this phenomenon is that, first, the large magnitude of pulse current injects the bundle with a significant amount of heat in a short period without overheating. Second, the slow cooling speed, as well as the visco-elasticity of the material, ensures that during the pulse intervals, the already actuated strain of the bundle is mostly preserved. Such periodic accumulation of actuation strain results in faster actuation strain rate (Figure 3d; Figure S9b, Supporting Information), larger actuation strain and stress (Figure 3e). However, the pulse heating method has little impact on the heat dissipation of the square knotted bundles, their recovery speed remains consistent with that actuated by continuous current (Figure S9c, Supporting Information). When the current frequency is higher than 0.1Hz, the higher current frequency leads to lower maximum current that the LCE fibers can withstand. This is because each heating periodic is long enough when the current frequency is lower than 0.1Hz, which accumulates a very high temperature that could melt the LCE. Therefore, the pulse current should not exceed 1.6A when the frequency is 5Hz, and the frequency should not be lower than 0.1Hz when the pulse current above 0.8A, to avoid melting of the LCE at temperature above 180°C.

The actuation performance of the square knotted bundle is then examined against different actuation frequencies, applied loads, and actuation cycle numbers. The actuation frequency is defined as the reciprocal of the power-on duration. When the actuation frequency is smaller than 0.07Hz, the actuation strain of square knotted bundle remains nominally constant at about 60%. When the actuation frequency increases to 1Hz, it retains a 10% actuation strain, which is already sufficient for many applications (Figure S10, Supporting Information). In Figure 3f, we examine the actuation force of a typical square knotted artificial muscle ranging from 1.27g (0.01N) to 20g (0.2N), up to 260 times of its own weight. In Figure S6 (Supporting Information), we show that by adding LCE fibers and heating threads, the actuation force of the proposed artificial muscle can easily scale up to 1.15N (762 times of self-weight), which already reaches the efficiency of human muscles (around 300–400 times of self-weight (Movie S5, Supporting Information).[57] The cycling durability is tested against 2000 cycles, using a pulse current of 1.6A at 5Hz (Figure 3g). The sample repeatedly contracts to 60% without any failure or notable variation (Figure S11, Supporting Information).In addition, we have also calculated the power density, cycle life, and energy conversion efficiency of the square knotted artificial muscle (see Supporting Information). These performance metrics exceed those of many other LCE-based artificial muscles.

We then systematically investigate the influence of pitch distance between knots (P) on the actuation performance of the square knotted artificial muscles. Under the same stimulation of 0.8A current, the square knotted artificial muscle with pitch of 4mm has the largest actuation strain of 53%. The actuation strain is only 15% when the LCE fibers are tightly braided with a pitch of 0mm (Figure 3h; Movie S6, Supporting Information). This reduction of actuation strain under tight braiding is also observed in previous literature.[12] Such a large difference highlights the importance of pitch distance in knotted artificial muscles, which has not caught enough attention before. When the pitch is small, LCE strands form an interlocking structure preventing further contraction of the artificial muscle. On the other hand, when the pitch is larger than 4mm, the loose bond between the heating threads and LCE fibers results in decreased heating efficiency, which further causes decreased actuation strain. Therefore, a 4mm-pitch is the optimal choice for the square knotted bundles.

Surprisingly, with the optimized design, the square knotted structure endows the artificial muscle with superior robustness to damage. The entanglement between LCE fibers prevents cascading failure of the knotted artificial muscle when several LCE fibers are broken. Hence, the functionality is maintained even when the artificial muscle is severely damaged. We investigate its actuation performance under various damage scenarios, as depicted in Figure 3i. Experiments show that the damaged artificial muscles exhibit very robust actuation (Figure 3j; Movie S7, Supporting Information). Even when all LCE fibers are broken, the artificial muscle still exhibits an actuation strain of more than 20%. Such excellent robustness is quite unique for underwater soft actuators, given that the DE actuators would completely fail once they are damaged even slightly.[19,20]

### 2.3. Underwater Actuation of the Square Knotted Artificial Muscles

Next, we explore the underwater performance of the square knotted artificial muscles. Being submerged in water, the square knotted artificial muscles continue to exhibit higher actuation strain compared to the other three types of artificial muscles (Figure S12; Movie S8, Supporting Information). Furthermore, the recovery speed of square knotted artificial muscle experiences a three-fold increase primarily due to the high thermal conductivity of water leading to quick dissipation of heat from the artificial muscle. On the other hand, such quick dissipation of heat, coupled with the high specific heat capacity of water, poses a challenge in achieving fast temperature rise of the submerged artificial muscle (Figure S13, Supporting Information). Meanwhile, we discover the pulse heating method is less effective underwater due to the reduced difference of actuation strain rate and recovery speed since water prohibits heat accumulation.

To compensate for the heating efficiency, we apply carbon coating on the LCE fibers (**Figure 4**a),[36] which results in a 10% increase of the actuation strain rate and 30% increase of the actuation strain underwater (Figure 4b,c; Movie S9, Supporting Information). The carbon coating is applied by brushing a layer of conductive carbon glue on the surface of the LCE fibers. According to the SEM images, the carbon coating is uniformly and tightly bonded with the surface of LCE fibers (Figure 4a). The resultant boost of performance is likely due to the improved absorption of thermal radiation, and the carbon coating on the knotted artificial muscles persists after 500 cycles of underwater actuation (Figure S14a,b, Supporting Information). Indeed, improved actuation performance due to carbon coating is also observed in air, on the actuation strain, actuation strain rate, actuation force, and force rate (Figure S15– 17; Movie S10, Supporting Information).

Moreover, we increase the numbers of LCE fibers and heating threads in the knotted bundle to further improve underwater actuation performance. As shown in Figure S16 (Supporting Information), using 16 LCE fibers in each strand results in an increased actuation strain of 23%, and an actuation strain rate of nearly 5%$s^{-1}$, subjected to a continuous current of 5A (Figure 4c). Because the maximal current that each heating thread can tolerate is 6A, the input power to the artificial muscle is limited. Therefore, we braid multiple heating threads into one square knotted bundle to boost the input power (Figure 4d). We observe that the actuation strain and strain rate reach their maxima of 32% and 19%$s^{-1}$, respectively, when there are five heating threads, each subject to 5A of current (Figure 4e,f; Movie S11, Supporting Information). The good news is that such large current would not burn out the heating threads, which cannot be achieved in air. As the number of parallel threads further increases, their stiffness begins to have a negative impact on the contraction of the bundles. As a result, the underwater actuation strain and strain rate do not increase any further.

### 2.4. Deepwater Actuation of the Square Knotted Artificial Muscles

We observe an actuation strain about 30% under 2MPa hydrostatic pressure with water temperature at 4°C (equivalent to 200m depth), which is not compromised compared to the shallow water experiments at 18°C. The input power is about 50W, nearly the same as in shallow water (Figure S16, Supporting Information). As the hydrostatic pressure increases to 10 and 30MPa, the actuation strain decreases to 16% and 8%, respectively (Figure 4g,h; Movie S12, Supporting Information). Even with the decreased actuation strain, the proposed artificial muscle still presents larger stroke compared to other polymeric based actuators underwater.[53] In addition, the artificial muscle performs reliable cycles of actuation under 1000m deepwater (Figure 4i).

To verify the effectiveness of the square knotted artificial muscles in underwater applications, we utilize one bundle to actuate a paddle. We attach one end of the bundle to a plastic film (i.e., the paddle), and the other end to a fixed pole (**Figure 5**a). When the electric current switches on and off, the square knotted bundle contracts and recovers, causing the film to flap up and down (Figure 5b). As shown in Figure 5b, in shallow water environment (10cm), the flapping angle reaches about 10° at 1Hz of actuation (Figure 5c). When the frequency drops to 0.2Hz, the flapping angle of the paddle increases to 15° (Figure 5d; Movie S13, Supporting Information). Besides shallow water environment, we also test this artificial muscle actuated paddle in deepwater environment.

As shown in Figure 5e, the square knotted artificial muscle bundle successfully actuates the paddle to flap in a pressure vessel subjected to hydrostatic pressures ranging from 2 to 30MPa,

ADVANCED MATERIALS
www.advmat.de

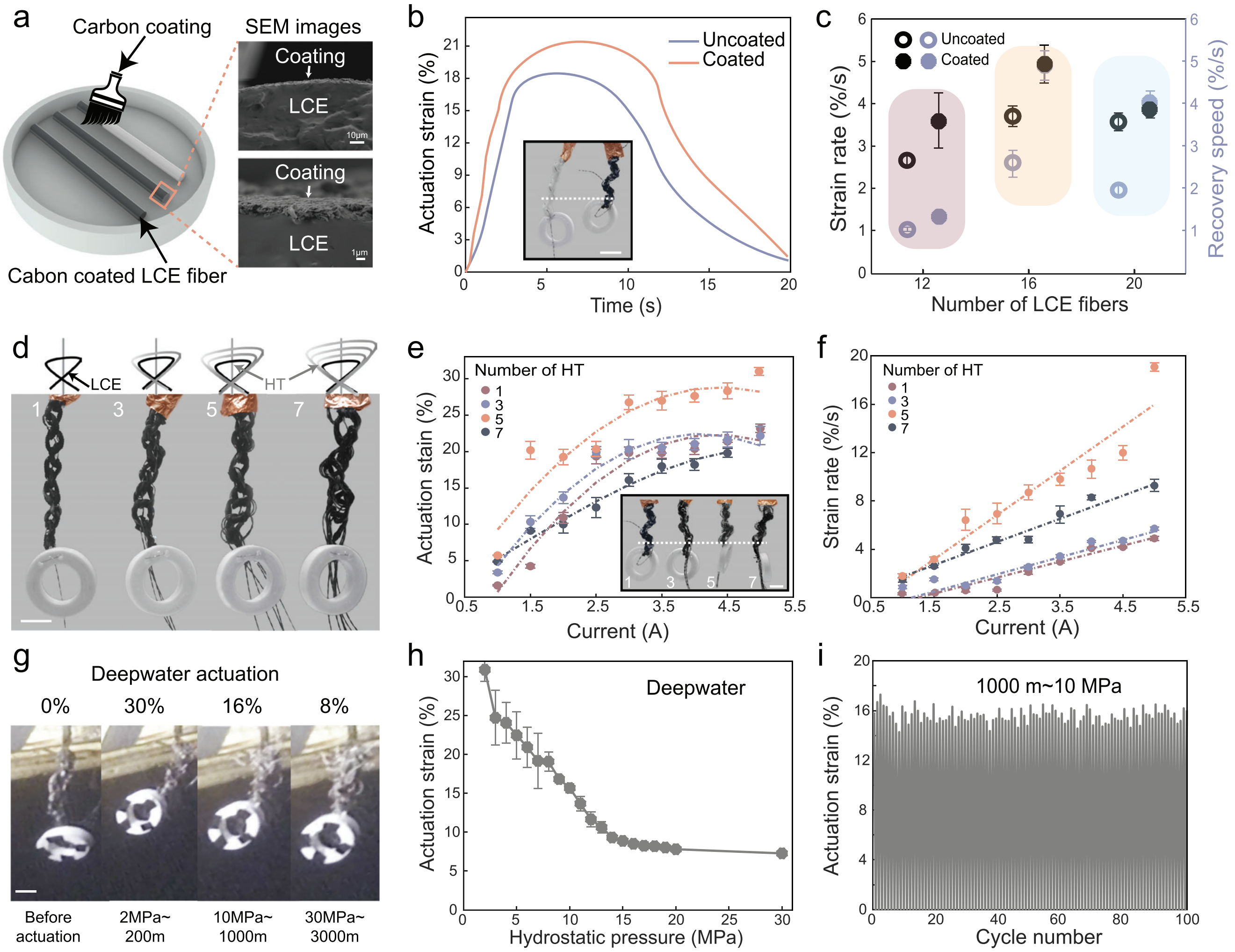


**Figure 4.** Optimization of underwater actuation performance. a) Carbon-coating of LCE fibers. The inset on the right is the SEM images of the interface between the carbon coating and LCE fiber. Comparison of artificial muscle bundles made of strands with different numbers (12, 16, 20) and treatments (uncoated, coated) of LCE fibers: b) The contraction and relaxation process of the square knotted bundle with and without carbon coating, powered by the same electric current (5A, continuous) from 0 to 10s. The insets are the contracted states of the coated and uncoated bundles. The scale bar is 1cm. c) Actuation strain rate and recovery speed. The error bars extend to one standard deviation. d) Schematics and photographs of square knotted bundles with different numbers of heating threads (HT). Comparison of artificial muscle bundles consisting of different numbers of heating threads under various input current (3-5A): e) Actuation strain, and f) actuation strain rate. The insets in (e) show the contracted states of the square knotted bundle with different numbers of heating threads (scale bar: 1cm). The error bars extend to one standard deviation. The dotdashed line in (e) refers to the fitted quadratic relationship, and the dotdashed line in (f) refers to the fitted linear relationship. Shallow water temperature: 18°C. g) Photographs of square knotted bundles before actuation, and actuated under hydrostatic pressure of 2MPa, 10MPa, and 30MPa. The scale bar is 10mm. h) The actuation strain of the square knotted bundle with a stimulation of 3.2A per heating thread under different hydrostatic pressures and the power is about 50W. i) 100 cycles of actuation with a 1g weight under hydrostatic pressure of 10MPa. Deepwater temperature: 4°C.

equivalent to water depths of 200 to 3000m (Figure S20, Supporting Information). As the hydrostatic pressure increases from 2 to 10MPa, the flapping angle of the paddle gradually decreases from 10° to 5°, stimulated by a electric current of 2.5A per heating thread at 1Hz (Figure S19a, Supporting Information). The corresponding actuation strain of the square knotted bundle decreases from 5% to 2%. The same current magnitude can hardly actuates the paddle when the pressure continues to increase. Therefore, for experiments under hydrostatic pressures from 10 to 30MPa, we increase the magnitude of the current to 3.4A per heating thread. Under 10MPa, the actuation strain of square knotted bundle increases to 5% and the flapping angle of the paddle increases to 8° (Figure 5f). As the hydrostatic pressure further increases to 20MPa, and even 30MPa, the paddle still exhibits reliable flapping action. The flapping angle gradually decreases to 5° (Figure 5g; Figure S21b, Supporting Information) to 3° (Figure 5h; Movie S14, Supporting Information).

Following a comprehensive study of the underwater actuation performance of the square knotted bundles, we then implement them in a demonstrative application: propelling of a boat (Figure 5i–j; Movie S15, Supporting Information), to further validate the effectiveness of the proposed artificial muscles for underwater applications. The square knotted bundle is attached to two paddles extending from the bottom of a 3D printed boat. With a

 

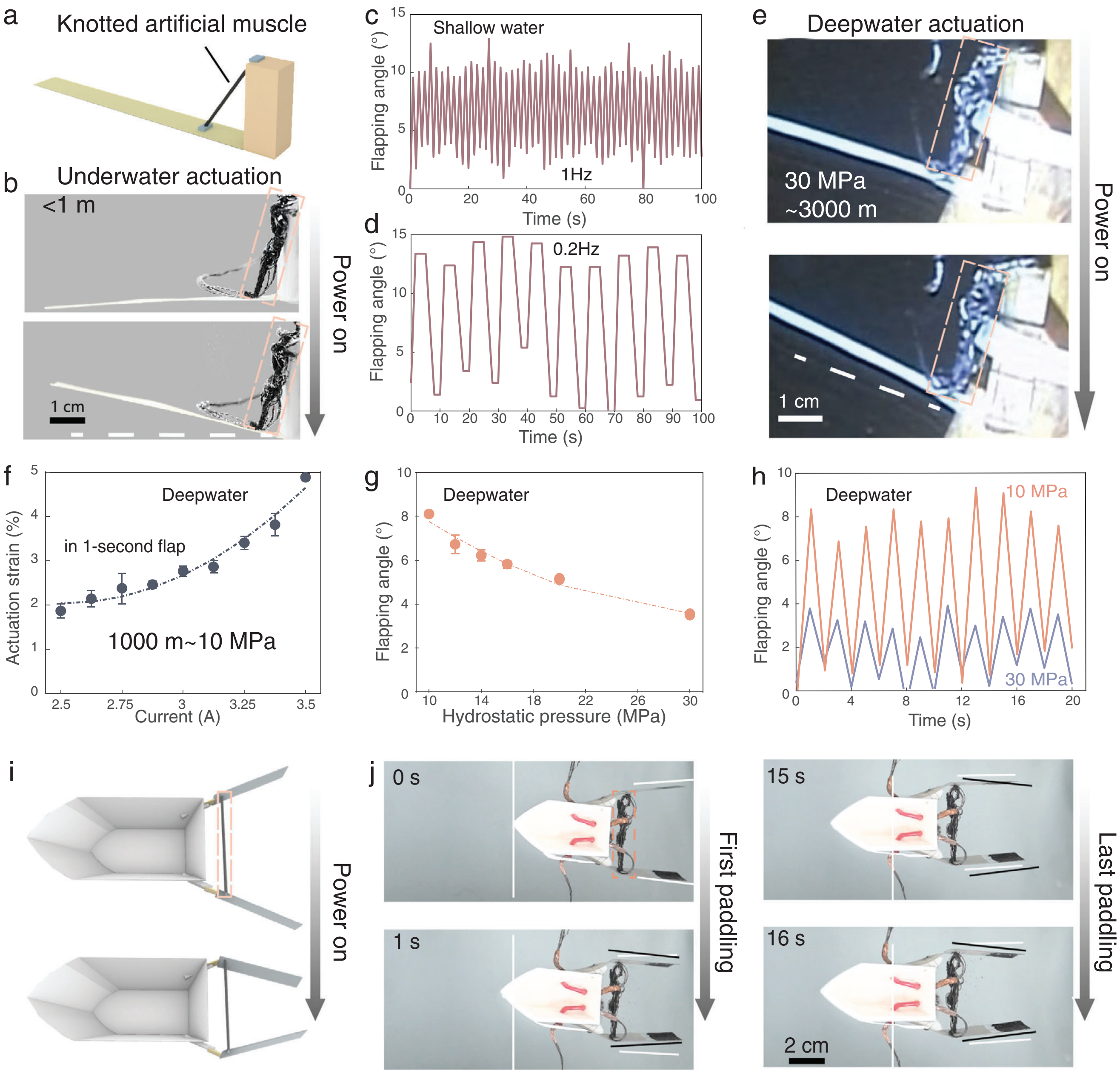


**Figure 5.** Underwater applications of the square knotted artificial muscle. a) Schematic of the flapping paddle setup. b) When the artificial muscle bundle contracts, the paddle flaps. c,d) presents the paddle flapping angle as a function of time for current frequency of 0.2Hz and 1Hz, respectively. e) Driven by the artificial muscle bundle, the paddle flaps in the pressure vessel with a hydrostatic pressure of 30MPa, which is equivalent to 3000m deep. f) The calculated actuation strain in one second of the artificial muscle bundle under 10MPa of pressure versus the magnitude of input current. g) The flapping angle of the paddle versus different hydrostatic pressures. The error bars extend to one standard deviation. The dotdashed lines in (f) and (g) refer to the fitted quadratic relationship. h) Influence of equivalent water depth on the cycling actuation of the artificial muscle bundle, reflected as the flapping angle. The maximum flapping angle decreases as the pressure increases from 10 to 30MPa, with current frequency of 1 Hz. i) Design of the boat model. j) Locomotion of the boat model, actuated by the artificial muscle bundle. In all panels, the orange boxes highlight the square knotted artificial muscle bundle.

pulse input current of 4A per heating thread at 1Hz, the flapping movement of the two paddles effectively pushes the boat moving forward at a speed of 0.7cms$^{-1}$. We note that this example is only used to demonstrate potential underwater applications, the design of the boat and the propelling method are not optimized for sailing speed.

## 3. Conclusion

In this work, we develop a convenient braiding scheme to produce artificial muscles with superior actuation performance using LCE, which marks the first LCE-based soft actuator capable of high stroke actuation in deepwater environment, down to an equivalent 3000m depth. Inspired by the hierarchical structure of natural muscles, we braid LCE fibers and heating threads into knotted bundles. Surprisingly, the knotted bundles exhibit larger actuation strain than that of the LCE fibers, especially for the square knot structure with a spiral topology after being actuated. Such spiral topology also leads to efficient heat absorption and dissipation, resulting in high frequency actuation with a strain rate up to 20%/s underwater. In addition, we would like to stress on the superior damage-tolerance of the knotted artificial muscles, achieving 20% contraction after all fibers are broken. Furthermore, the knotted artificial muscles exhibit reliable actuation cycles in both air and water, exemplified by a boat propelling experiment. These unique advantages, especially the high stroke and robustness, are pivotal for biomimetic underwater robotics, emulating the linear and soft muscular structures of aquatic fauna. Looking ahead, the knotted artificial muscles may be mass manufactured using industrial machines, and its reliable and adaptable performance promises great potential for applications in virtual reality experiences, minimally invasive surgeries, water quality monitoring, and deep-sea exploration.

## 4. Experimental Section

Detailed procedures are provided in the Supporting Information.

*Preparation of the LCE Ink*: LCE ink was made by mixing (1,4-Bis-[4-(3-acryloyloxypropyloxy) benzoyloxy]-2-methylbenzene) (RM257) (Wilshire Technologies,95%), EDDET (Sigma–Aldrich, 95%), dipropylamine (Sigma-Aldrich, 98%), (2-hydroxyethoxy)-2-methylpropiophenone (Irgacure 2959, Sigma-Aldrich, 98%), RhB (Sigma–Aldrich), and methylene chloride (Sinopharm, CH2Cl2). RM257 (HWRK Chem, 8.2404g, 14mmol) was dissolved in 50ml of dichloromethane. Then, chain extender EDDET (2.1876g, 12mmol) and catalyst dipropylamine (0.100–0.500g, 1 –5mmol) were added into the mixture dropwisely. The solution was stirred at room temperature overnight. After that, a photoinitiator (Irgacure 651, Medkoo, 0.0500g, 0.2mmol) was added into the solution. into the solution. Then, the mixture was left in an oven of 85°C for 24 h to allow complete evaporation of the solvent.

*Fabrication of the Knotted Bundles*: LCE ink was loaded into a syringe and the syringe was loaded on a customized direct ink writing 3D printer. Then, LCE fibers were printed with a speed of 2mms$^{-1}$ at room temperature of 25°C. The flow rate was controlled by regulating the air pressure. After printing, fibers were removed from build plate and placed under a UV lamp of 365nm wavelength for 1 h curing. Artificial muscle bundles were manually braided with multiple strands of LCE fibers and the heating threads.

*Characterization of the LCE Ink*: The DSC measurements were conducted using a Discovery DSC250 instrument (TA Instruments) under a nitrogen atmosphere. The heating and cooling processes were performed at a scanning rate of 40°Cmin$^{-1}$, spanning a temperature range from -20°C to 200°C (Figure S1, Supporting Information). The rheological characterization of LCE ink was conducted using the MCR 302 Rheometer (Anton Paar). All experiments were conducted with a 20-mm steel Peltier plate and 0.5-mm gap size. The oscillatory tests were conducted with a fixed frequency of 1Hz.

*Characterization of the Printed LCE*: The optical images and videos were taken using a camera (Sony). The POM images were taken using a ZEISS polarized microscope. Experiments of thermally induced actuation of printed LCE fibers were conducted with a hot plate. All samples were heated from 30° to 120°C at a rate of about 24°Cmin$^{-1}$. The uni-axial mechanical testes were conducted on a Universal Mechanical Testing System (Series F, Mark-10) with a 50N loading cell. The LCE samples were tested as printed with diameter of 250mm and length of 30mm. The stretching speed was set to be 5mmmin$^{-1}$ for the mechanical tests.

*Actuation Characterization*: A precision variable adjustable power supply (2200-50-3, ITECH) was used as the power source for the knotted artificial muscle bundles. Position and actuation were tracked by either digital video or time lapse photography, using MATLAB. The temperature change during the actuation process was measured by an infrared thermal camera (PS400, GUIDE INFRARED). The water temperature during shallow water actuation experiments was 18°C.

*Characterization of the Bonding between the Carbon Coating and the LCE Fiber*: A coated LCE fiber was submerged in liquid nitrogen and then broken to create a fractured cross-section, which reveals the bonding interface between the LCE fiber and the carbon coating. The fractured cross-section was examined by a scanning electron microscope (ZEISS, GeminiSEM 300). The SEM image of the bonding interface between LCE fiber and carbon particles shows that the carbon coating was uniformly and tightly placed on top of the surface of the LCE fibers (Figure 4a).

*Deepwater Actuation Experiment*: The paddle actuated by knotted artificial muscle bundle was mounted on a deep-sea lander during the field test in the pressure vessel (Figure S17a,b, Supporting Information). The lander was then put into a pressure vessel full of water by a crane (Figure S17c, Supporting Information). In this pressure vessel, the hydrostatic pressure was gradually increased from 2 to 30MPa with a rate of 1MPamin$^{-1}$, and the hydrostatic pressure was kept at each level for 10 min. Electric threads that attached on the artificial muscle bundle was extended and connected to external power supplies through the sealed outlet of the pressure vessel. Experimental processes were recorded using protected video cameras and LEDs attached to the lander.

*Numerical Simulation*: The numerical simulations were based on the Discrete Elastic Rod (DER) model, which was utilized to capture the deformation process of the artificial muscle bundles with various braiding styles. The details of numerical simulations of knotted artificial muscles are presented in the Supporting Information.

## Supporting Information

Supporting Information is available from the Wiley Online Library or from the author.

## Acknowledgements

This research was supported by the National Key Research and Development Program of China through grant 2022YFB4701900, the National Natural Science Foundation of China through grant 12372159, and the Fundamental Research Funds for the Central Universities, Peking University. The Analytical Instrumentation Center of Peking University was acknowledged for the measurements of DSC. The authors thank Prof. Lianqing Liu from Shenyang Institute of Automation for helpful discussions during the research. The authors also thank Ms. Biru Tang for suggestions on the visualization.

## Conflict of Interest

The authors declare no conflict of interest.

## Author Contributions

W.C., K.L., C.W., and H.Y. designed the research. W.C., L.M., and R.L. performed all experiments. W.C. and B.T. performed data analysis. D.T. conducted the theoretical derivations and numerical simulations. K.L. supervised the project. All the authors participated in the analysis of the results and in the writing of the paper.

## Data Availability Statement

The data that support the findings of this study are available from the corresponding author upon reasonable request.

## Keywords

artificial muscles, deepwater application, knot structure, liquid crystal elastomer, soft actuator

Received: January 15, 2024
Revised: March 7, 2024
Published online:

[1] M. Shi, E. Yeatman, *Microsyst. Nanoeng.* **2021**, *7*, 95.
[2] J. Madden, N. Vandesteeg, P. Anquetil, P. Madden, A. Takshi, R. Pytel, S. Lafontaine, P. Wieringa, P. Wieringa, *IEEE J. Ocean. Eng.* **2004**, *29*, 706.
[3] M. Kanik, S. Orguc, G. Varnavides, J. Kim, T. Benavides, D. Gonzalez, T. Akintilo, C. C. Tasan, A. P. Chandrakasan, Y. Fink, P. Anikeeva, *Science* **2019**, *365*, 145.
[4] M. D. Lima, N. Li, M. J. de Andrade, S. Fang, J. Oh, G. M. Spinks, M. E. Kozlov, C. S. Haines, D. Suh, J. Foroughi, S. J. Kim, Y. Chen, T. Ware, M. K. Shin, L. D. Machado, A. F. Fonseca, J. D. W. Madden, W. E. Voit, D. S. Galvão, R. H. Baughman, *Science* **2012**, *338*, 928.
[5] C. S. Haines, M. D. Lima, N. Li, G. M. Spinks, J. Foroughi, J. D. W. Madden, S. H. Kim, S. Fang, M. J. de Andrade, F. Göktepe, Ö. Göktepe, S. M. Mirvakili, S. Naficy, X. Lepró, J. Oh, M. E. Kozlov, S. J. Kim, X. Xu, B. J. Swedlove, G. G. Wallace, R. H. Baughman, Science **2014**, *343*, 868.
[6] V. Magdanz, M. Medina-Sanchez, L. Schwarz, H. Xu, J. Elgeti, O. G. Schmidt, *Adv. Mater.* **2017**, *24*, 1606301.
[7] H. Chu, X. Hu, Z. Wang, J. Mu, N. Li, X. Zhou, S. Fang, C. S. Haines, J. W. Park, S. Qin, N. Yuan, J. Xu, S. Tawfick, H. Kim, P. Conlin, M. Cho, K. Cho, J. Oh, S. Nielsen, K. A. Alberto, J. M. Razal, J. Foroughi, G. M. Spinks, S. J. Kim, J. Ding, J. Leng, R. H. Baughman, *Science* **2021**, *6528*, 494.
[8] W. Pang, S. Xu, J. Wu, R. Bo, T. Jin, Y. Xiao, Z. Liu, F. Zhang, X. Cheng, K. Bai, H. Song, Z. Xue, L. Wen, Y. Zhang, *P. Natl. Acad. Sci. USA* **2022**, *119*, e2215028119.
[9] D. Kim, B. Kim, B. Shin, D. Shin, C.-K. Lee, J.-S. Chung, J. Seo, Y.-T. Kim, G. Sung, W. Seo, S. Kim, S. Hong, S. Hwang, S. Han, D. Kang, H.-S. Lee, J.-S. Koh, *Nat. Commun.* **2022**, *1*, 4155.
[10] J. Wu, S. Yao, H. Zhang, W. Man, Z. Bai, F. Zhang, X. Wang, D. Fang, Y. Zhang, *Adv. Mater.* **2021**, *33*, 2106175.
[11] K. W. Kwan, S. J. Li, N. Y. Hau, W.-D. Li, S. P. Feng, A. H. W. Ngan, *Sci. Robot.* **2018**, *18*, eaat4051.
[12] X. Wang, H. Shao, J. Tang, J. Chen, Y. Huang, J. Pan, Y. Zhang, W. Wang, J. Jiang, N. Chen, *Adv. Mater. Technol.* **2023**, *8*, 2300814.
[13] S. M. Mirvakili, D. Sim, R. Hunter, Ian W.and Langer, *Sci. Robot.* **2020**, *41*, eaaz4239.
[14] Y. Ling, L. Li, J. Liu, K. Li, C. Hou, Q. Zhang, Y. Li, H. Wang, *Adv. Mater.* **2023**, *36*, 2305914.
[15] Q. Zhao, H. J. Qi, T. Xie, *Prog. Polym. Sci.* **2015**, *49-50*, 79.
[16] Y. Xia, Y. He, F. Zhang, Y. Liu, J. Leng, *Adv. Mater.* **2020**, *33*, 2000713.
[17] H. Na, Y.-W. Kang, C. S. Park, S. Jung, H.-Y. Kim, J.-Y. Sun, *Science* **2022**, *376*, 301.
[18] Y. S. Zhang, A. Khademhosseini, *Science* **2017**, *356*, eaaf3627.
[19] Y. Shi, E. Askounis, R. Plamthottam, T. Libby, Z. Peng, K. Youssef, J. Pu, R. Pelrine, Q. Pei, *Science* **2022**, *377*, 228.
[20] C. Tang, B. Du, S. Jiang, Q. Shao, X. Dong, X.-J. Liu, H. Zhao, *Sci. Robot.* **2022**, *7*, eabm8597.
[21] Q. Wang, L. Yu, M. Yu, D. Zhao, P. Song, H. Chi, L. Guo, H. Yang, *Macromol. Rapid Commun.* **2017**, *38*, 1600699.
[22] H. Wermter, H. Finkelmann, *e-Polymers* **2001**, *1*, 013.
[23] R. Bai, K. Bhattacharya, *J. Mech. Phys. Solids* **2020**, *144*, 104115.
[24] Y. Wang, Q. He, Z. Wang, S. Zhang, C. Li, Z. Wang, Y.-L. Park, S. Cai, *Adv. Mater.* **2023**, *35*, 2211283.
[25] W. Hou, J. Wang, J. an Lv, *Adv. Mater.* **2023**, *35*, 2211800.
[26] Y. Geng, D. Sim, R. Hunter, Ian W.and Langer, *Nat. Mater.* **2022**, *21*, 1441.
[27] H. Kim, J. M. Boothby, S. Ramachandran, C. D. Lee, T. H. Ware, *Macromolecules* **2017**, *50*, 4267.
[28] S. Wu, Y. Hong, Y. Zhao, J. Yin, Y. Zhu, *Sci. Adv.* **2023**, *9*, eadf8014.
[29] Q. He, Z. Wang, Y. Wang, Z. Wang, C. Li, R. Annapooranan, J. Zeng, R. Chen, S. Cai, *Sci. Robot.* **2021**, *6*, eabi9704.
[30] Y. Zhao, Y. Chi, Y. Hong, Y. Li, S. Yang, J. Yin, *P. Natl. Acad. Sci. USA* **2022**, *119*, e2200265119.
[31] V. Maurin, Y. Chang, Q. Ze, S. Leanza, J. Wang, R. R. Zhao, *Adv. Mater.* **2023**, 2302765.
[32] O. M. Wani, H. Zeng, A. Priimagi, *Nat. Commun.* **2017**, *8*, 15546.
[33] B. Ni, G. Liu, M. Zhang, M. Tatoulian, P. Keller, , M.-H. Li, *ACS Appl. Mater. Inter.* **2021**, *13*, 54439.
[34] M. J. Ford, C. P. Ambulo, T. A. Kent, E. J. Markvick, C. Pan, J. Malen, T. H. Ware, C. Majidi, *P. Natl. Acad. Sci. USA* **2019**, *116*, 21438.
[35] A. Kotikian, J. Morales, A. Lu, J. Mueller, Z. Davidso, J. Boley, J. Lewis, *Adv. Mater.* **2021**, *33*, 2101814.
[36] M. Chambers, H. Finkelmann, M. Remškar, A. Sánchez-Ferrer, B. Zalar, S. Žumer, *J. Mater. Chem.* **2009**, *19*, 1524.
[37] M. M. Porter, A. Vandervoort, J. Lexell, *Scand. J. Med. Sci. Spor.* **1995**, *5*, 129.
[38] Y. Wang, W. Liao, J. Sun, R. Nandi, Z. Yang, *Adv. Mater. Technol.* **2022**, *7*, 2100934.
[39] P. E. S. Silva, X. Lin, M. Vaara, M. Mohan, J. Vapaavuori, E. M. Terentjev, *Adv. Mater.* **2023**, *35*, 2210689.
[40] X. Peng, S. Wu, X. Sun, L. Yue, S. M. Montgomery, F. Demoly, K. Zhou, R. R. Zhao, H. J. Qi, *Adv. Mater.* **2022**, *34*, 2204890.
[41] Y. Zhao, Q. Li, Z. Liu, Y. Alsaid, P. Shi, M. K. Jawed, X. He, *Sci. Robot.* **2023**, *8*, eadf4753.
[42] S. Palagi, A. G. Mark, S. Y. Reigh, K. Melde, T. Qiu, H. Zeng, C. Parmeggiani, D. Martella, A. Sanchez-Castillo, N. Kapernaum, F. Giesselmann, D. S. Wiersma, E. Lauga, P. Fischer, *Nat. Mater.* **2016**, *15*, 647.
[43] Y. Wang, Q. Guan, D. Lei, R. E. Neisiany, Y. Guo, S. Gu, Z. You, *ACS Nano* **2022**, *16*, 19393.
[44] M. Camacho-Lopez, H. Finkelmann, P. Palffy-Muhoray, M. Shelley, *Nat. Mater.* **2004**, *3*, 307.
[45] H. Shahsavan, A. Aghakhani, H. Zeng, Y. Guo, Z. S. Davidson, A. Priimagi, M. Sitti, *P. Natl. Acad. Sci. USA* **2020**, *117*, 5125.
[46] H. Tian, Z. Wang, Y. Chen, J. Shao, T. Gao, S. Cai, *ACS Appl. Mater. Inter.* **2018**, *10*, 8307.
[47] T. Zhao, Y. Zhang, Y. Fan, J. Wang, H. Jiangb, J. an Lv, *J. Mater. Chem. C* **2022**, *10*, 3796.
[48] J. Zhang, Y. Guo, W. Hu, R. H. Soon, Z. S. Davidson, M. Sitti, *Adv. Mater.* **2022**, *33*, 2006191.
[49] J. D. Isaacs, R. A. Schwartzlose, *Sci. Am.* **1975**, *233*, 84.
[50] J. A. Koslow, *Am. Sci.* **1997**, *85*, 168.
[51] H. J. T. Hoving, S. H. Haddock, *Sci. Rep.* **2017**, *7*, 44952.
[52] T. Kawabata, D. J. Lindsay, M. Kitamura, S. Konishi, J. Nishikawa, S. Nishida, M. Kamio, H. Nagai, *Chem. Biochem.* **2013**, *79*, 487.
[53] G. Li, X. Chen, F. Zhou, Y. Liang, Y. Xiao, X. Cao, Z. Zhang, M. Zhang, B. Wu, S. Yin, Y. Xu, H. Fan, Z. Chen, W. Song, W. Yang, B. Pan, J. Hou, W. Zou, S. He, X. Yang, G. Mao, Z. Jia, H. Zhou, T. Li, W. Yang, *Nature* **2021**, *591*, 66.
[54] H. Chu, X. Hu, Z. Wang, J. Mu, N. Li, X. Hou, S. Fang, CarterS.Haines, J. Park, S. Qin, N. Yuan, J. Xu, S. Tawfick, H. Kim, P. Conlin, M. Cho, J. Oh, S. Nielsen, KevinA.Alberto, J. Razal, J. Foroughi, G. M.

 

Spinks, S. J. Kim, J. Ding, J. Leng, R. H. Baughman, *Science* **2021**, *371*, 494.
[55] J. Cui, Y. S. Chu, O. O. Famodu, Y. Furuya, J. Hattrick-Simpers, R. D. James, A. Ludwig, S. Thienhaus, M. Wuttig, Z. Zhang, I. Takeuchi, *Nat. Mater.* **2006**, *5*, 286.
[56] Y. Y. Huang, J. Biggins, Y. Ji, E. M. Terentjev, *J.Appl. Phys.* **2010**, *107*, 083515.
[57] J. E. Hall, *Guyton and Hall Textbook of Medical Physiology*, 13th ed., Guyton and Hall Textbook of Medical Physiology, Elsevier, Philadelphia **2016**.

 